AGU PUBLICATIONS

JGR

Journal of Geophysical Research: Space Physics

RESEARCH ARTICLE
10.1002/2015JA021826

Key Points:
- We present ion temperature-dependent models of energetic neutral atom scattering off lunar regolith
- ENA scattering fraction from lunar regolith is ~10% in the magnetosheath
- ENA images show plasma wakes downstream of magnetic anomalies near terminator

Correspondence to:
C. Lue,
charles.lue@irf.se

Citation:
Lue, C., Y. Futaana, S. Barabash, Y. Saito, M. Nishino, M. Wieser, K. Asamura, A. Bhardwaj, and P. Wurz (2016), Scattering characteristics and imaging of energetic neutral atoms from the Moon in the terrestrial magnetosheath, *J. Geophys. Res. Space Physics*, *121*, 432–445, doi:10.1002/2015JA021826.

Received 31 AUG 2015
Accepted 24 DEC 2015
Accepted article online 29 DEC 2015
Published online 30 JAN 2016

Scattering characteristics and imaging of energetic neutral atoms from the Moon in the terrestrial magnetosheath

Charles Lue[1,2], Yoshifumi Futaana[1], Stas Barabash[1], Yoshifumi Saito[3], Masaki Nishino[4], Martin Wieser[1], Kazushi Asamura[3], Anil Bhardwaj[5], and Peter Wurz[6]

[1]Swedish Institute of Space Physics, Kiruna, Sweden, [2]Department of Physics, Umeå University, Umeå, Sweden, [3]Institute of Space and Astronautical Science, Japan Aerospace Exploration Agency, Sagamihara, Japan, [4]Solar-Terrestrial Environment Laboratory, Nagoya University, Nagoya, Japan, [5]Space Physics Laboratory, Vikram Sarabhai Space Center, Trivandrum, India, [6]Physikalisches Institut, University of Bern, Bern, Switzerland

Abstract We study hydrogen energetic neutral atom (ENA) emissions from the lunar surface, when the Moon is inside the terrestrial magnetosheath. The ENAs are generated by neutralization and backscattering of incident protons of solar wind origin. First, we model the effect of the increased ion temperature in the magnetosheath (>10 times larger than that in the undisturbed solar wind) on the ENA scattering characteristics. Then, we apply these models to ENA measurements by Chandrayaan-1 and simultaneous ion measurements by Kaguya at the Moon, in the magnetosheath. We produce maps of the ENA scattering fraction, covering a region at the lunar near-side that includes mare and highland surfaces and several lunar magnetic anomalies. We see clear signatures of plasma shielding by the magnetic anomalies. The maps are made at different lunar local times, and the results indicate an extended influence and altered morphology of the magnetic anomalies at shallower incidence angles of the magnetosheath protons. The scattering fraction from the unmagnetized regions remains consistent with that in the undisturbed solar wind (10%–20%). Moreover, the observed ENA energy spectra are well reproduced by our temperature-dependent model. We conclude that the ENA scattering process is unchanged in the magnetosheath. Similarly to the undisturbed solar wind case, it is only magnetic anomalies that provide contrast in the ENA maps, not any selenomorphological features such as mare and highland regions.

1. Introduction

Recent lunar orbiters have observed scattering of solar wind protons from the lunar surface back into interplanetary space. A fraction of ~0.1%–1% of the solar wind protons incident on the lunar surface are scattered maintaining their positive charge [*Saito et al.*, 2008; *Lue et al.*, 2014], while ~10%–20% of the incident protons are scattered in the form of energetic neutral atoms (ENAs) of hydrogen by collecting an electron from the lunar surface during the scattering process [*McComas et al.*, 2009; *Wieser et al.*, 2009].

Imaging of the scattered ENAs has proven to be a very useful tool for remote-sensing of the plasma precipitation onto the lunar surface [e.g., *Wieser et al.*, 2010; *Vorburger et al.*, 2012, 2013; *Futaana et al.*, 2013]. By mapping the ENA emissions and comparing them to the upstream solar wind flux, it is possible to observe remotely how the solar wind flow to the surface is modified on a local scale by lunar crustal magnetic anomalies [*Futaana et al.*, 2006]. By recording the ENA energy spectrum, it is even possible to measure remotely the lunar surface potential [*Futaana et al.*, 2013]. Studies have also investigated the correlation between the ENA scattering fraction and lunar surface properties [*Vorburger et al.*, 2013, 2015], but no correlations with any surface properties other than local magnetization were identified.

Previous lunar ENA imaging studies [*Wieser et al.*, 2010; *Vorburger et al.*, 2012, 2013, 2015; *Futaana et al.*, 2013] have included high-resolution (a few degrees longitude/latitude) selenographic maps of the ENA reflection, but they were performed when the Moon was situated in the undisturbed solar wind, upstream of the Earth's bow shock. However, it is also important to extend these studies to the cases when the Moon is in the terrestrial magnetosheath so as to investigate the effect of the increased plasma temperature on the plasma interaction with the Moon (e.g., interaction with magnetic anomalies or nightside plasma precipitation) and to complete the ENA imaging of the lunar near-side, which is mostly exposed to magnetosheath plasma and contains most of the lunar mare regions.

We first have to address the change of the ENA scattering properties due to the ion temperature to enable ENA imaging in the magnetosheath. The ENA scattering function in the solar wind was studied by

Schaufelberger et al. [2011], and the ENA energy spectrum in the solar wind has been studied by *Futaana et al.* [2012] and *Rodríguez et al.* [2012]. *Funsten et al.* [2013] presented simulation results of the scattering function and energy spectrum for a solar wind-like incident beam.

Allegrini et al. [2013] compared ENA scattering in the solar wind with that in the magnetosheath and observed a broadening of the ENA energy spectrum and an increased scattering efficiency. These were global observations given the vantage point of the Interstellar Boundary Explorer (IBEX), of about 10^5 km distance from the Moon. They investigated different possible explanations for the increased scattering efficiency: (1) an effect of the uncertainty of the incident plasma parameters in the magnetosheath, modeled by the BATS-R-US magnetosphere model; (2) a difference between mare and highland regions; or (3) an effect of the broader distribution of the incident protons. They found the latter explanation most plausible. On the other hand, ENA observations by the Chandrayaan-1 lunar orbiter in the solar wind [e.g., *Futaana et al.*, 2012] and in the magnetosheath [e.g., *Wieser et al.*, 2009] both reported ENA scattering fractions of ~20%, suggesting that the scattering fraction does not change between these plasma regions. As a more extreme example of increased ion temperature, we can compare with observations in the plasma sheet, where *Harada et al.* [2014] obtained an ENA scattering fraction of $<$10% of the incident plasma sheet protons. Despite large differences in the incident proton distribution between *Futaana et al.* [2012], *Wieser et al.* [2009], and *Harada et al.* [2014], the resulting ENA spectra were similar. Thus, the studies referenced in this paragraph give quite different pictures of the quantitative and qualitative changes of the ENA scattering properties as a function of the ion temperature.

In the present study, we use the empirical ENA scattering models developed by *Schaufelberger et al.* [2011] and *Futaana et al.* [2012] for the solar wind case and adapt them to account for the velocity distribution function of the magnetosheath protons. Then, we use these models together with ENA and ion observations by the Chandrayaan-1 and Kaguya lunar orbiters to produce ENA images of a region on the lunar near side, including both mare and highland regions as well as areas with crustal magnetization. We also compare the temperature-dependent scattering models to our ENA observations and discuss the observations by *Allegrini et al.* [2013] and *Harada et al.* [2014] in light of the model results.

2. Models

We model the direct effects that an increased ion temperature is expected to have on the ENA scattering from the Moon: (1) the modification of the global plasma precipitation (and thus the ENA emission pattern), (2) the modification of the ENA energy spectrum, and (3) the modification of the ENA scattering function.

We evaluate the impinging proton flux on the lunar surface J_{in} as the product of the upstream proton number density, n, and the velocity component directed into the surface ($-v \cdot \hat{\boldsymbol{r}}$). To account for a proton distribution with a given bulk velocity, v_b, and temperature, kT, we multiply the above product with the velocity distribution $f_{\boldsymbol{v}}(\boldsymbol{v}; v_b, kT)$ (normalized to unity), and integrate over all directions not blocked by the lunar surface:

$$J_{in} = n \iiint_{\hat{v} \cdot \hat{r} < 0} (-\boldsymbol{v} \cdot \hat{\boldsymbol{r}}) \cdot f_{\boldsymbol{v}}(\boldsymbol{v}; v_b,\ kT)\ dv_x dv_y dv_z. \quad (1)$$

Figure 1a shows the resulting proton precipitation onto the lunar surface as a function of the plasma zenith angle (PZA) for three different distribution functions, representing common conditions in the solar wind, magnetosheath, and plasma sheet, respectively. The solar wind is approximated as a drifting Maxwellian distribution (v_b = 400 km/s, kT = 10 eV), the plasma sheet is approximated as a stationary Maxwellian distribution (0 km/s, 600 eV), and the magnetosheath is approximated as a drifting Kappa distribution (300 km/s, 200 eV, κ = 2). The magnetosheath kappa value is chosen based on results from *Formisano et al.* [1973]. We use the PZA to get $-\hat{v} \cdot \hat{\boldsymbol{r}}$. It is analogous to the commonly used solar zenith angle (SZA), but accounts for the deviation of the bulk plasma flow from the anti-Sun direction. Note that the precipitating flux is the projection onto the surface normal of the downgoing part of the ambient omnidirectional flux [cf. *Carron*, 2007]. Therefore, the precipitating fraction at the subsolar point decreases from the solar wind to the magnetosheath case. We can also see that the precipitating flux reaches $\frac{1}{2} \cdot \cos(60°) = \frac{1}{4}$ of the omnidirectional flux for a fully thermalized incident distribution (the first half represents the blockage of half the distribution by the lunar surface, and 60° is the mean incidence angle of the remaining distribution).

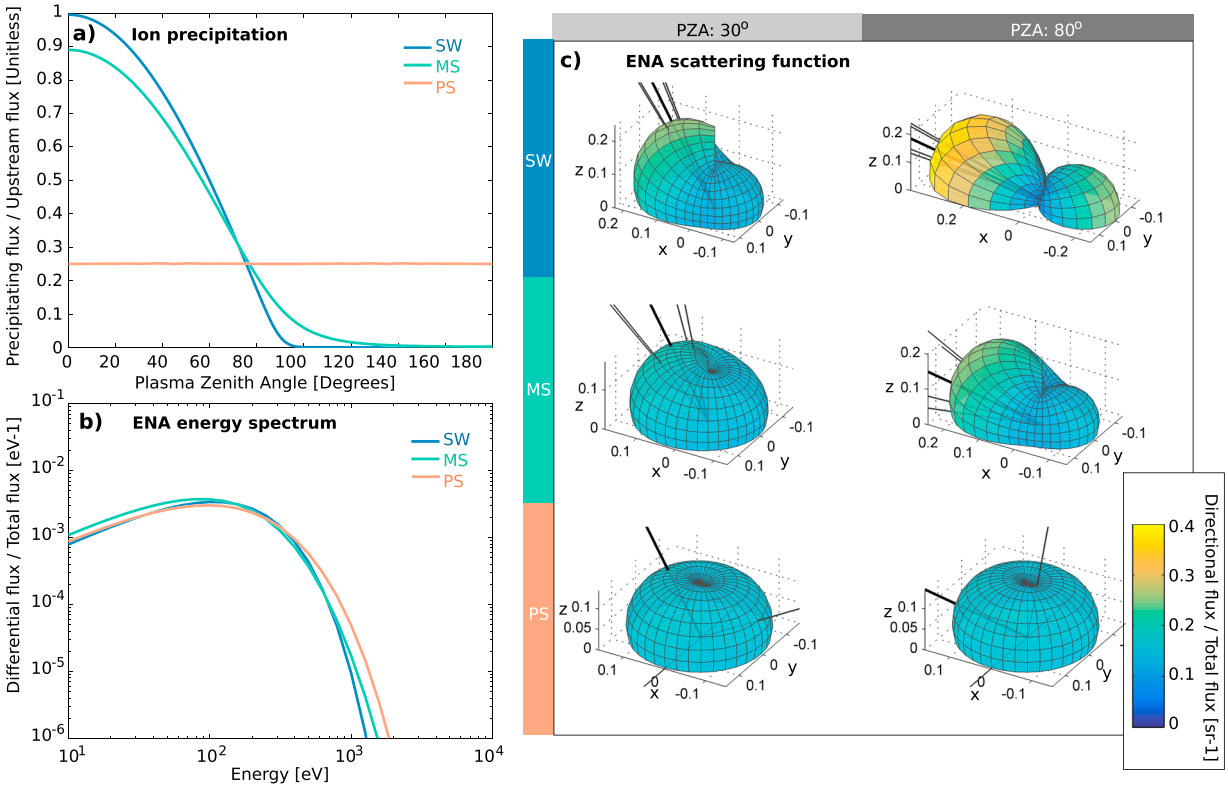

Figure 1. The modeled effect of different plasma ion conditions on (a) the precipitating ion flux (equation (1)), divided by the omnidirectional upstream flux; (b) derived models of the scattered ENA energy spectrum (equation (7)): scattered ENA flux, differentiated in energy, normalized to unity, and calculated for a plasma-zenith angle (PZA; i.e., bulk incidence angle) of 60°; and (c) the ENA directional scattering function (equation (11)), shown for 30° and 80° PZA. Three different incident ion distributions are used in the models, representing typical conditions for the undisturbed solar wind (SW: 400 km/s, 0 eV), the magnetosheath (MS: 300 km/s, 200 eV), and the plasma sheet (PS, 0 km/s, 600 eV), respectively. (The bulk speed and ion plasma temperature are given in parentheses.) In Figure 1c, the black lines indicate the incident ion bulk direction and, for illustration of the temperature, directions within a cone of arctan(thermal speed/bulk speed). The radius in the frame marked with *x*, *y*, *z* (*z* is toward zenith, and *x* is antiparallel to the surface projection of the ion bulk velocity), and the color of the surfaces both show the ENA flux, differentiated in angular space, normalized to unity.

The ENA energy spectrum has been modeled empirically by *Futaana et al.* [2012] and *Rodríguez et al.* [2012]. Here we use the model by *Futaana et al.* [2012], describing the scattered ENAs as a Maxwellian distribution:

$$f_{v.\,\mathrm{ENA}}(v_{\mathrm{ENA}}; kT_{\mathrm{ENA}}) = 4\pi\left(\frac{m_p}{2\pi kT_{\mathrm{ENA}}}\right)^{\frac{3}{2}} v_{\mathrm{ENA}}^2 \exp\left[\frac{-m_p v_{\mathrm{ENA}}^2}{2kT_{ENA}}\right], \tag{2}$$

where the parameter kT_{ENA}, i.e., the effective temperature of the backscattered ENAs, was found to be linear to the incident solar wind speed v_{sw} (expressed in km/s) as

$$kT_{\mathrm{ENA}}(v_{sw}) = 0.273\ \frac{\mathrm{eV}\cdot s}{\mathrm{km}} \cdot v_{sw} - 1.99\,\mathrm{eV}. \tag{3}$$

This model of the ENA energy spectrum was obtained in the low-temperature solar wind. Therefore, we consider it applicable in representing the ENA response for a singular incidence speed v_i. We then convolve it with the incident plasma velocity distribution to get a new, temperature-dependent expression for the ENA distribution ($g_{v.\,\mathrm{ENA}}$):

$$g_{v.\,\mathrm{ENA}}(v_{\mathrm{ENA}}; v_b,\ kT) = \frac{\iiint_{\hat{\boldsymbol{v}}_i\cdot\hat{\boldsymbol{r}}<0} f_{v.\,\mathrm{ENA}}(v_{\mathrm{ENA}}; kT_{\mathrm{ENA}}(v_i))\cdot f_{\boldsymbol{v}}(\boldsymbol{v_i}; v_b,\ kT)\cdot(-\boldsymbol{v_i}\cdot\hat{\boldsymbol{r}})\ dv_x dv_y dv_z}{\iiint_{\hat{\boldsymbol{v}}_i\cdot\hat{\boldsymbol{r}}<0} f_{\boldsymbol{v}}(\boldsymbol{v_i}; v_b,\ kT)\cdot(-\boldsymbol{v_i}\cdot\hat{\boldsymbol{r}})\ dv_{ix} dv_{iy} dv_{iz}}, \tag{4}$$

where the denominator is added for normalization to unity. Conversion to energy space is done by

$$g_{E.\,\mathrm{ENA}}(E_{\mathrm{ENA}}; v_b,\ kT_{ms}) = g_{v.\,\mathrm{ENA}}(v_{\mathrm{ENA}}; v_b,\ kT)\cdot\frac{dv_{\mathrm{ENA}}}{dE_{\mathrm{ENA}}} = \sqrt{\frac{1}{2m_pE_{\mathrm{ENA}}}}\,g_{v.\,\mathrm{ENA}}\left(\sqrt{\frac{2E_{\mathrm{ENA}}}{m_p}}; v_b,\ kT\right). \tag{5}$$

We then convert equation (5) to differential flux. We do not yet address the scattering efficiency or directional scattering function but express the normalized differential flux (h_E):

$$h_E(E_{\mathrm{ENA}}; v_b,\ kT) = \frac{\sqrt{\frac{2E_{\mathrm{ENA}}}{m_p}}\,g_{E.\,\mathrm{ENA}}(E_{\mathrm{ENA}}; v_b,\ kT)}{\int_{E>0}\sqrt{\frac{2E_j}{m_p}}\,g_{E.\,\mathrm{ENA}}(E; v_b,\ kT)dE}. \tag{6}$$

Inserting equation (5) in equation (6) gives

$$h_E(E_{ENA}; v_b,\ kT) = \frac{g_{v.\,\mathrm{ENA}}\left(\sqrt{\frac{2E_{\mathrm{ENA}}}{m_p}}; v_b,\ kT\right)}{\int_{E>0} g_{v.\,\mathrm{ENA}}\left(\sqrt{\frac{2E}{m_p}}; v_b,\ kT\right)dE}. \tag{7}$$

The modeled normalized ENA energy spectra for different plasma temperatures are shown in Figure 1b.

Next, we address the ENA scattering function. An empirical ENA scattering function was obtained from Chandrayaan-1 data by *Schaufelberger et al.* [2011] as

$$f_s(az, el;\ \mathrm{SZA}) = f_0(\ \mathrm{SZA})\cdot f_1(az;\ \mathrm{SZA})\cdot f_2(az;\ \mathrm{SZA})\cdot f_3(el;\ \mathrm{SZA}), \tag{8}$$

where *az* and *el* are the azimuth and elevation of the scattering direction, and f_1, f_2, and f_3 are given by *Schaufelberger et al.* [2011]. We use the updated f_0 given by *Vorburger et al.* [2013]. The updated f_0 is designed to ensure that

$$\int_0^{\pi}\int_0^{2\pi} f_0f_1f_2f_3\cos(el)dazdel = \cos(\ \mathrm{SZA}), \tag{9}$$

i.e., f_s is normalized to cos(SZA), to account for the relation between incident flux onto the surface and upstream flux. As we use a separate precipitation function, we normalize the scattering function to unity, giving the following expression for the ENA scattering function in the solar wind:

$$g_s(az, el;\ \mathrm{SZA}) = \frac{f_s(az, el;\ \mathrm{SZA})}{\cos(\ \mathrm{SZA})}, \tag{10}$$

where f_s is the expression in (8). The azimuth *az* and solar zenith angle SZA (which we replace with PZA) are defined from the incident particle trajectory. Thus, we convolve this function with the precipitating plasma velocity distribution function, to get a new scattering function (h_s):

$$h_s(az, el;\ \mathrm{PZA}, v_b, kT) = \frac{\iiint_{\hat{\boldsymbol{v}}\cdot\hat{\boldsymbol{r}}<0} g_s(\alpha(\hat{\boldsymbol{v}},\hat{\boldsymbol{r}}), el; \sigma(\hat{\boldsymbol{v}},\hat{\boldsymbol{r}}))\cdot f_{\boldsymbol{v}}(\boldsymbol{v}; v_b,\ kT)\cdot(-\boldsymbol{v}\cdot\hat{\boldsymbol{r}})\,dv_xdv_ydv_z}{\iiint_{\hat{\boldsymbol{v}}\cdot\hat{\boldsymbol{r}}<0} f_{\boldsymbol{v}}(\boldsymbol{v}; v_b,\ kT)\cdot(-\boldsymbol{v}\cdot\hat{\boldsymbol{r}})\,dv_xdv_ydv_z}, \tag{11}$$

where α and σ are the modified *az* and PZA. The denominator in (11) is for normalization to unity. Examples of the resulting scattering function can be seen in Figure 1c.

With these models, measurements of *n*, v_b, and *kT* of the magnetosheath ions, and a reflection fraction η, we can derive expectation values for the ENA differential fluxes j_{dE}, for specific scattering angles and energies:

$$j_{dE} = \eta\cdot J_{in}(\ \mathrm{PZA}; n, v_b, kT)\cdot h_E(E;\ \mathrm{PZA}, v_b, kT)\cdot h_s(az, el;\ \mathrm{PZA}, v_b, kT). \tag{12}$$

3. Observations

We use data from the Chandrayaan-1 and Kaguya spacecraft to study the ENA scattering from the Moon in the magnetosheath, applying and testing the above models. To monitor backscattered ENAs, we use the Chandrayaan-1 Energetic Neutrals Analyzer (CENA) [*Kazama et al.*, 2007]. To study the incident ions, we use data from two ion sensors: the Ion Energy Analyzer (IEA) [*Saito et al.*, 2010] on Kaguya and the Solar Wind Monitor (SWIM) [*McCann et al.*, 2007] on Chandrayaan-1. The respective instrument properties are listed in Table 1.

Table 1. Instrument Properties

	SWIM[a]	CENA[b]	IEA[c]
Field of view	7° × 160° (~nadir to zenith)	10° × 160° (centered at nadir)	2π sr (centered at zenith)
Angular resolution	7° × 10°	10° × 25°	5° × 5°
Energy range	100 eV–3 keV	10 eV–3.3 keV (here: 38–652 eV)	7 eV–29 keV
Energy resolution	7%	100%	5%

[a] *McCann et al.* [2007].
[b] *Kazama et al.* [2007].
[c] *Saito et al.* [2010].

Two periods were identified for which ENA data from Chandrayaan-1 and ion data from Kaguya are both available and during which the Moon was in the magnetosheath: The first period (P1) on 12 April 2009 00:07–02:05 and the second period (P2) on 5 June 2009 02:14–10:10. The two spacecraft had circular polar orbits, with orbital periods of ~2 h. Period P1 corresponds to a single orbit for either spacecraft. During P1, Chandrayaan-1 had an altitude of ~100 km and its orbital plane was near the day-night terminator, while Kaguya had an altitude of ~50 km and an orbital plane close to noon-midnight configuration (Figure 2a). Period P2 corresponds to three orbits, with Chandrayaan-1 near noon-midnight orbit at ~200 km altitude and Kaguya near the terminator at ~50 km altitude (Figure 2b). Figure 2c shows that the Moon is within the nominal magnetosheath region (this is confirmed by our plasma measurements; see next paragraph). Figures 2d and 2e show that the two spacecraft were over the lunar dayside simultaneously for large parts of the periods. Additionally, the ground tracks of the Chandrayaan-1 orbits were at almost the same selenographic longitude for the two periods (Figure 2f), thus allowing observations of the same region on the Moon at two different ion precipitation conditions.

In Figures 3 and 4, we show Chandrayaan-1 and Kaguya observations for P1 and P2, respectively. We show the downgoing plasma observed by the IEA sensor (Figures 3a and 4a), which has the largest coverage around the Sun direction and is the least disturbed by other ion populations such as reflected protons from the Moon [e.g., *Saito et al.*, 2010: *Lue et al.*, 2011]. To potentially detect significant local differences between the plasma at Kaguya and that at Chandrayaan-1, we also show SWIM data of precipitating ions (Figures 3b and 4b), although it does not cover the full angular distribution of the magnetosheath ions because of its

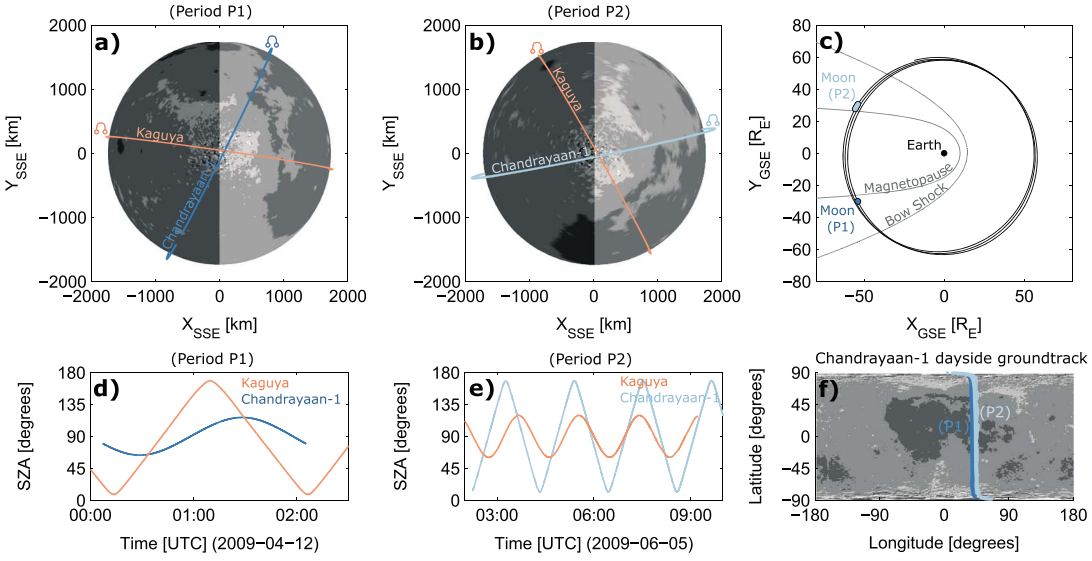

Figure 2. The orbits of Chandrayaan-1 (dark/light blue) and Kaguya (orange) during (a) Period 1 and (b) Period 2. Ascending node symbols indicate the ascending nodes. (c) The Moon position during Period 1 (dark blue) and Period 2 (light blue), along with typical boundaries for the terrestrial bow shock [*Fairfield*, 1971] and magnetopause [*Shue et al.*, 1997]. (d and e) Subsatellite solar zenith angles during Period 1 and 2, respectively, and (f) the Chandrayaan-1 ground-track in the selenographic coordinate system, for both periods. The lunar topography is illustrated by a simplified lunar albedo map (original Clementine image data from www.nrl.navy.mil/clementine).

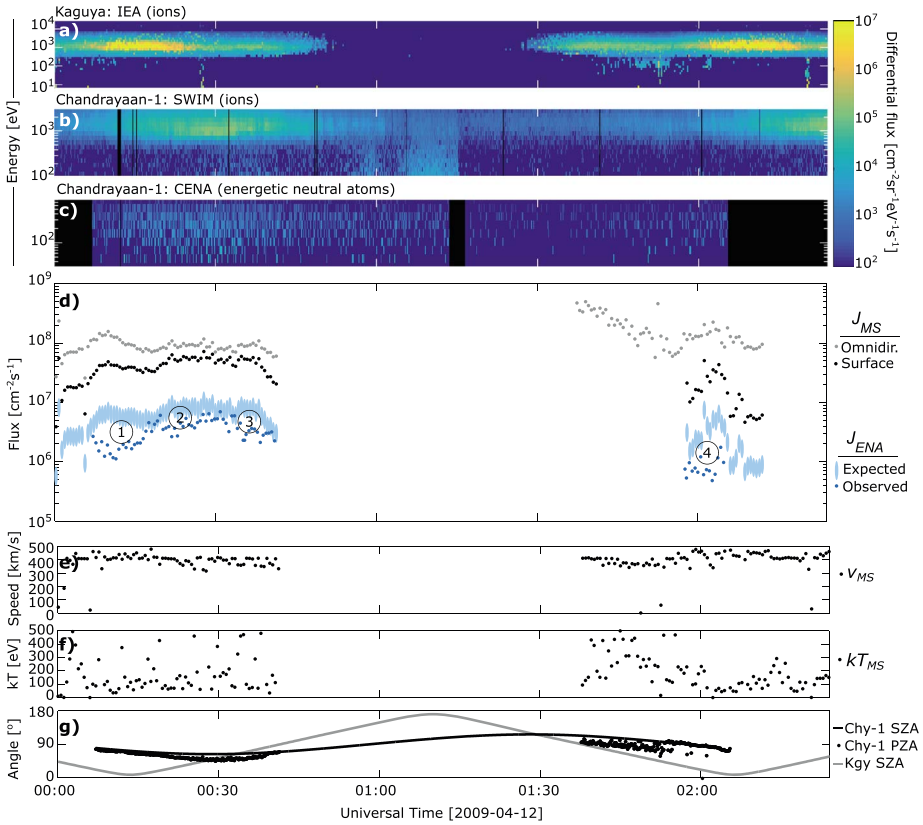

Figure 3. Kaguya and Chandrayaan-1 observations during Period 1. Ion energy spectrograms, from (a) IEA on Kaguya and (b) SWIM on Chandrayaan-1. (c) Energetic neutral atom (ENA) energy spectrogram, from CENA on Chandrayaan-1. In the spectrograms, black indicates missing data. (d) Magnetosheath proton flux J_{MS} (omnidirectional), measured by IEA; and ENA flux J_{ENA}, observed by CENA. For comparison between these fluxes, we also show the estimated flux incident on the lunar surface under Chandrayaan-1 (J_{MS}: Surface), and the 10%–20% level of this (J_{ENA}: Expected), which represents the expected level of the ENA flux. (e) Magnetosheath proton speed, measured by IEA. (f) Magnetosheath proton temperature, measured by IEA. (g) Subsatellite solar zenith angle (SZA) for both Chandrayaan-1 and Kaguya and, for Chandrayaan-1, the plasma zenith angle (PZA), which accounts for deviations in the plasma bulk flow from the anti-Sun direction. Numbered circles in Figure 3d highlight significant disagreements between the expected and observed ENA flux.

narrow aperture. To focus on the precipitating ions, we only plot SWIM data from the zenith half of its field of view. We use the full CENA field of view to study the scattered ENAs (Figures 3c and 4c).

To estimate the magnetosheath plasma parameters, we fit the sum of two Kappa distributions, representing protons and alpha particles to the IEA spectrum. To improve the stability of the fitting procedure, we reduce the number of free parameters. Instead of allowing κ to be a free parameter, we use $\kappa = 2$, which has been found to well reproduce observed magnetosheath proton distributions [*Formisano et al.*, 1973]. We assume the alpha bulk speed and temperature to be the same as the values for the protons, and we constrain the alpha density to a value within 1%–10% of the proton density. We plot the resulting magnetosheath proton flux, speed, and temperature in Figures 3d–3f and 4d–4f. Overviewing the two periods, we see that the incident magnetosheath flux during P1 is rather constant, at about 10^8 cm^{-2} s^{-1} (Figure 3d) with a bulk speed of ~400 km/s (Figure 3e) and a varying temperature on the order of 100 eV (Figure 3f). During P2, we see a highly variable magnetosheath plasma (~10^6–10^8 cm^{-2} s^{-1}, 100–300 km/s, tens to hundreds of eV, Figures 4d–4f). Using the plasma precipitation model (equation (1)) with the measured plasma parameters by Kaguya, we estimate the precipitating flux (Figures 3d and 4d) on the lunar surface under Chandrayaan-1, by accounting for the plasma zenith angle (Figures 3g and 4g) of the CENA footprint. This means that the surface flux shown in these figures is approximately the product of the magnetosheath flux and the cosine of the Chandrayaan-1 PZA, although we use the more precise equation (1). We then plot the expected ENA flux, at 10%–20% of the precipitating flux (Figures 3d and 4d). Finally, we plot the observed ENA flux by CENA. The scattered ENA flux

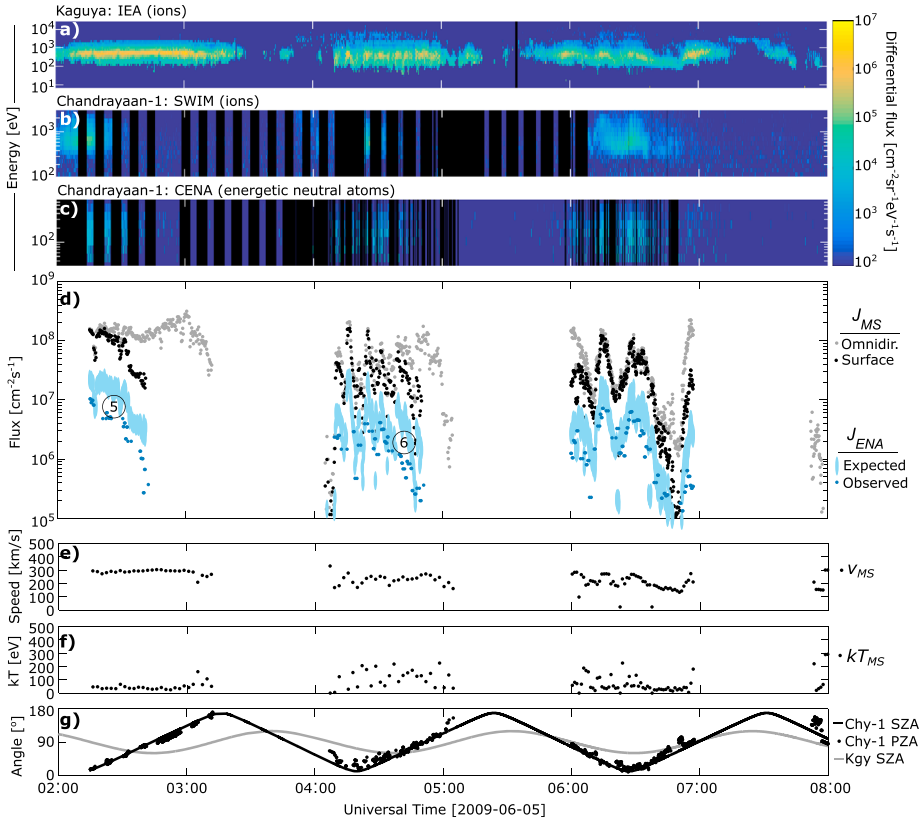

Figure 4. Kaguya and Chandrayaan-1 observations during Period 2. See detailed panel description in Figure 3. The labels (5) and (6) highlight significant disagreements between the expected and observed ENA flux.

is calculated by integrating the observed ENA energy spectrum and using the scattering model (equation (11)) to extrapolate the total scattered flux from the observation at a single scattering direction. We also subtract the expected background contribution. The CENA background is probably caused by UV photons and depends on the solar zenith angle. Using a subsequent orbit inside the lobe (not shown), where the plasma densities are very low, we estimate the (dayside) background to 0.3 $\cos^2$(SZA) counts per energy-direction bin

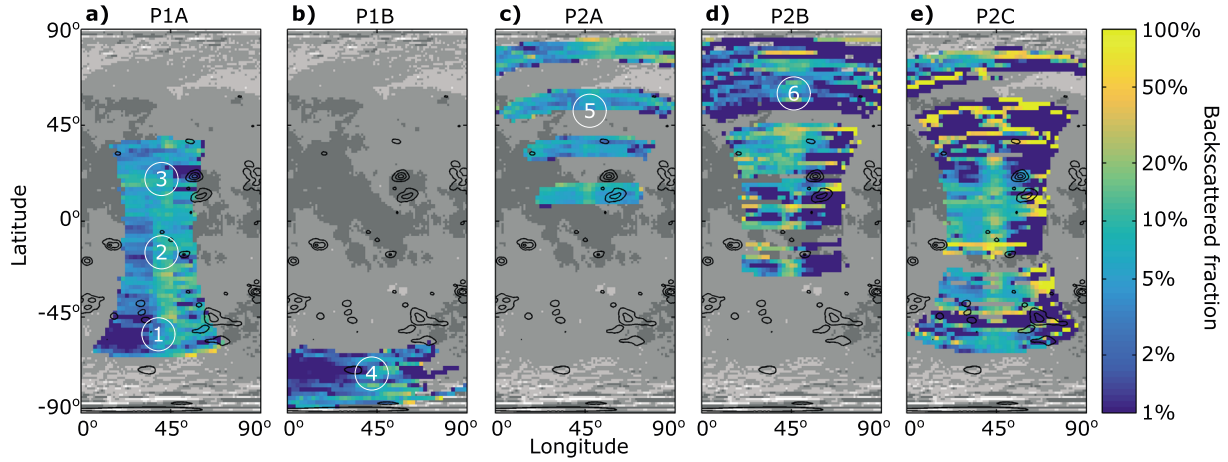

Figure 5. Selenographic maps of the ENA scattering fraction, for each of the orbits used in this study (P1A and P1B of Period 1 and P2A-C of Period 2). A simplified lunar albedo map (Clementine image data from www.nrl.navy.mil/clementine) and lunar crustal field contours (from the empirical magnetic field model by *Purucker and Nicholas* [2010]) are added for reference. The numbered circles mark the subsatellite points at the observation times labeled with the same numbers in Figures 3 and 4.

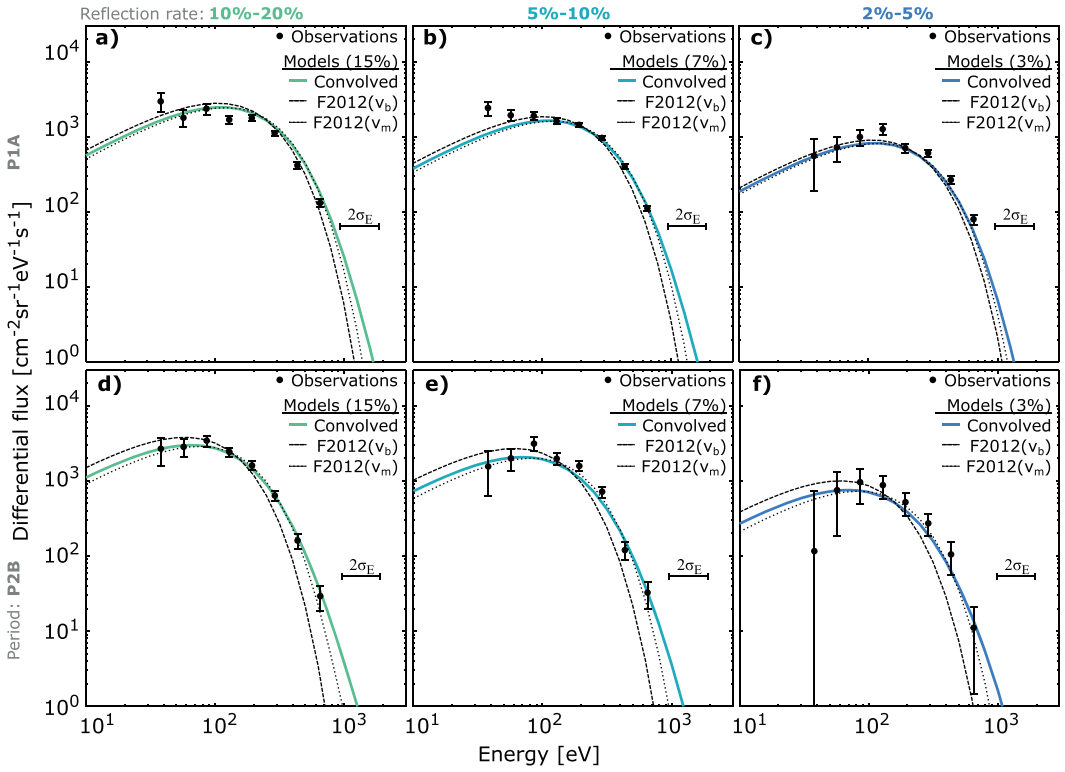

Figure 6. ENA energy spectra for orbits P1A and P2B (cf. Figure 5). The observations have been grouped by the scattering fraction into three groups ([10%–20%], [5%–10%], and [2%–5%]), based on the results shown in Figure 5. In each panel, we show modeled spectra from three different implementations of the model from *Futaana et al.* [2012]: The "convolved" model (equation (7)); the original, "F2012" model (equation (2)) as a function of the proton bulk speed v_b; and F2012 as a function of the proton mean speed v_m. For comparison with the observations, the model scattering rates are set to 15%, 7%, and 3%, respectively. The energy bins of the CENA sensor have approximately the same relative resolution, shown with the horizontal error bar ($2\sigma_E$). The vertical error bars show the standard deviations from count rate statistics.

per minute. This subtracted signal corresponds to an estimated ENA flux on the order of $10^6\,cm^{-2}\,s^{-1}$, and the effect is only significant at ~06:40–06:50 in P2.

We see a clear correlation between the observed and expected ENA fluxes in Figures 3d and 4d. The large fluctuations in the incident flux in P2 are well followed by the scattered ENA flux (Figure 4d 06:00–07:00). However, the scattering fraction is found to be mostly at the lower end of the expected range of 10%–20% and at several occasions (numbered 1–6 in the figures) much lower than 10%. These deviations have no clear correlation with the magnetosheath speed or temperature.

To further investigate the variations in the ENA scattering fraction, we make selenographic maps of the ENA scattering fraction (scattered ENA flux per incident plasma flux). We produce one map for each orbit (Figure 5) so that temporary effects can be distinguished. We identify three different types of deviations from the expected scattering fraction: (i) selenographically distinct features of decreased scattering fraction, observed in P1 (near the labels (1–4) in Figure 5; corresponding to the observation times marked as (1–4) in Figure 4); (ii) uniform decreases (i.e., they are clearly observed in the time series of Figure 4, but no clear spatial feature is seen in Figure 5) in P2 (marked as (5–6) in Figures 4 and 5); and (iii) regions where the signal-to-noise ratio is too low for the chosen spatial resolution of the map (where the expected ENA flux corresponds to less than one observed count; identified as intermittently blue and yellow regions in Figures 5d and 5e). The features of the first type listed above show decreases of the scattered ENA flux down to $<2\%$ of the incident flux, i.e., about 10 times less than the expected scattered flux.

We proceed by comparing the observed ENA energy spectra with the expectations from our model (equation (6)). We show a series of spectra in Figure 6 to investigate qualitative differences between the regions/times of high, medium, and low scattering fractions (as identified in Figure 5). We also investigate differences between the

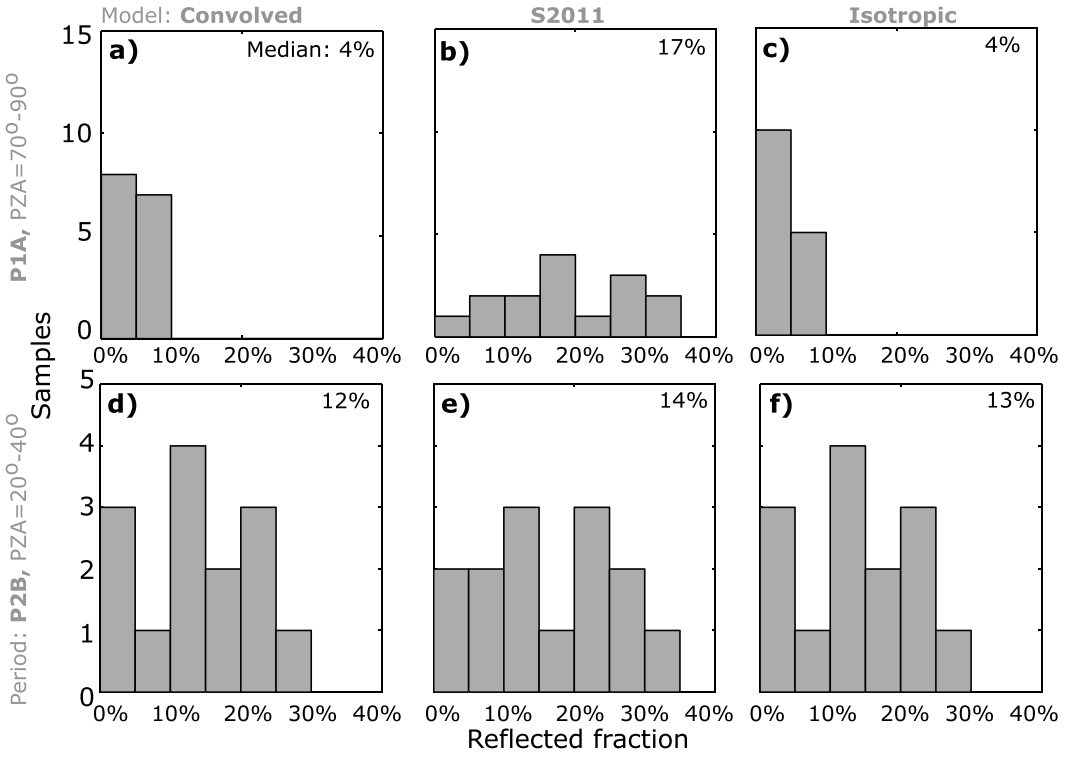

Figure 7. Histograms over ENA reflection fractions, calculated using three different models: the convolved model (equation (11)), the original model developed for the solar wind by *Schaufelberger et al.* [2011] (equation (10)) and an isotropic model (assuming: total scattered flux = $2\pi \cdot$ observed directional flux). (a–c) Data for plasma zenith angles of 70°–90°, selected from orbit P1A, and (d–f) data for plasma zenith angles of 20°–40°, selected from orbit P2B. The median values are also shown.

terminator- and noon-midnight cases, by showing the results from one orbit from P1 (P1A) and one orbit from P2 (P2B). The observed spectra agree well with our model for both periods, and this qualitative agreement is maintained regardless of the differences in the quantitative estimate for the scattering fraction. The original model developed for the regular solar wind (equation (2)), predicts a lower ENA energy spectrum than the observations show, if we use the bulk speed ($v_{sw} = v_b$) as the model input. If we instead use the proton mean speed, approximated here as

$$v_{sw} = v_m = \left(v_b{}^2 + 3kT/m_p\right)^{0.5}, \tag{13}$$

in equation (2), we get a closer match with the observations. A difference between the results of the convolved model and the latter adaptation is that the convolved model shows larger intensity toward higher and lower energies. However, the observations cover only the middle energies.

To further investigate the ENA scattering fraction and to evaluate the scattering function dependency, we plot histograms (Figure 7) of the scattering fraction estimates from P1A and P2B, for the different scattering models: the convolved model (equation (11)); the scattering model derived for the solar wind by *Schaufelberger et al.* [2011] (S2011; equation (10)); and the simple assumption of a uniform scattering function. The latter assumption has been used by, e.g., *Futaana et al.* [2012] for scattering at low solar-zenith angles, and Figure 1c shows that the increased temperature of the magnetosheath should make the convolved model closer to isotropic. In the histograms of Figure 7, each sample in the histogram represents a 1 min integration of the ENA measurements in one of the three central directional channels of CENA. These three channels have smaller surface footprints than the more sideward looking directions, resulting in a reduced uncertainty and spread in the scattering location and scattering angles of the measured particles. This processing is equivalent of investigating the central paths in Figures 5a and 5d. Further, we confined the data set for the histograms to specific ranges of incidence angles: PZA = 20°–40° and PZA = 70°–90°, to study the effect of the scattering model separately for low and high incidence angles. In the low PZA case

(Figure 7d), the median reflection fraction is between 10%, while in the high PZA case (Figure 7a), the values are mostly lower than 10%. (Note that this case also includes the large local decreases seen in Figure 5a.) By comparing Figures 7d–7f, we see that the choice of scattering function has a relatively small effect on the scattering fraction estimates at low PZA. In Figures 7a–7c, we see that the choice of scattering models is much more significant in the high PZA (grazing incidence) case. Not accounting for the plasma temperature (Figure 7b) gives a much higher scattering fraction, with a median above 20%, while the isotropic assumption gives a median $<5\%$.

4. Discussion

We observe an ENA scattering efficiency of ~10% (see Figures 3 and 4) as was established in the earlier studies [e.g., *Vorburger et al.*, 2013, Table 2], with the exception of certain deviations that we discuss later in this section. The scattering efficiency reported in this work is valid for the energy range 38–652 eV, while the full ENA spectrum extends further, and thus, the scattering efficiency integrated over the whole energy range down to thermal energy may be higher. The energy integration range can slightly affect the quantitative estimates of the scattering fraction. Our observations suggest an unchanged or lower scattering fraction in the magnetosheath compared to the previous reports in the solar wind. This is in disagreement with the increase in ENA flux observed by IBEX in the magnetosheath [*Allegrini et al.*, 2013]. These differences may be explained by the typical viewing geometries of Chandrayaan-1 and IBEX. The precipitation and scattering models obtained here can explain why higher ENA fluxes are emitted in the direction of IBEX in the magnetosheath even without an overall increase in the scattering efficiency. IBEX typically views the Moon in a direction perpendicular to the incident ion flow. From such a vantage point, the observed lunar surface receives more plasma precipitation if the plasma temperature increases (Figure 1a). This was also discussed by *Allegrini et al.* [2013], but they found that this effect alone could not explain the increased ENA flux, and they suggested a change of the scattering function. As seen in Figure 1c (and discussed by *Schaufelberger et al.* [2011]), ENAs are mainly backscattered toward the source, or almost specularly scattered forward, i.e., not favoring scattering directions perpendicular to the incident beam (toward the vantage point of IBEX) [cf. *Saul et al.*, 2013]. However, with increasing plasma temperature, the distribution of incidence angles becomes more isotropic, as does the resulting convolved scattering function (Figure 1c). This means that the portion scattered toward IBEX will increase significantly with temperature. This discussion is analogous to the discussion by *Allegrini et al.* [2013] about the microscopic-level scattering. Thus, our results qualitatively support that interpretation, which they proposed as one possible explanation for their observations. The quantitative effect can be investigated using Figure 7. The same directional flux that gives a total scattering fraction of 17% using the S2011 model (Figure 7b) gives only 4% using the isotropic model (Figure 7c). Conversely, this means that, for a constant scattering fraction, the directional flux toward an observer at high PZA in the solar wind (according to the S2011 model) is only 23% (=4/17) of the directional flux that would be expected for an isotropic scattering function. However, when the Moon enters the magnetosheath and the scattering function changes according to the convolved model, the directional flux toward the observer is almost the same as that expected for an isotropic function (compare Figures 7a and 7c). Thus, these results suggest that the directional flux to an observer over the terminator increases by a factor 4 in the magnetosheath only from the effect of the scattering function. This is quantitatively consistent with the results from *Allegrini et al.* [2013, ff. 10], which suggest a temperature-dependent increase by a factor of about 2–10. Therefore, we suggest that there is probably not an overall increase in the scattering efficiency but rather an altered directional scattering function generating an observational bias. The lower scattering fraction observed in the plasma sheet by *Harada et al.* [2014] and the present study in the magnetosheath (4%–12%), when compared to other Chandrayaan-1 observations in the solar wind (11%–21% [*Vorburger et al.*, 2013]; 16%–21% [*Futaana et al.*, 2012]), may be to some extent the opposite effect of this bias: The central viewing direction of CENA on Chandrayaan-1 sees ENAs scattered toward the zenith, which is a scattering direction that becomes less favorable with increasing plasma temperatures at least at low PZA (Figure 1c). This can explain the slightly higher value from *Futaana et al.* [2012], using isotropic assumption, compared to *Vorburger et al.* [2013], using their scattering model. Another effect on the observations by *Harada et al.* [2014]; *Vorburger et al.* [2013], and this study is the presence of strong magnetic anomalies along the Chandrayaan-1 ground-track, which are avoided by *Futaana et al.* [2012] by focusing on areas near the equator. It is also possible that the total scattering fraction decreases at grazing impact angles due to surface blocking of a part of the strong back scattering lobe

of the scattering function. Finally, there is a possibility that our convolved scattering model overcompensates for the temperature, because it assumes that the regular solar wind scattering model applies to a 0 eV incident plasma, although the solar wind has a finite temperature of ~10 eV already. We see in Figure 7 that the choice of scattering model strongly affects the resulting scattering fraction estimate at high PZA. If our model is overcompensating, then the real scattering fractions should be higher than our results in Period 1. Further work is required to resolve these issues. It is especially important to further constrain the temperature-dependence of the scattering function at high PZA, because it strongly affects ENA mapping efforts in these conditions.

In our ENA images, the features that are confined to certain selenographic regions (features (1–4) in Figures 3 and 5) show no correlation with mare/highland regions but are likely attributable to lunar magnetic anomalies. This is in agreement with the results by *Vorburger et al.* [2012, 2013, 2015] that no selenomorphological or compositional properties are visible in the ENA maps but only the effects of the lunar magnetic anomalies. The magnetic anomalies partially screen off and deviate the impinging plasma [e.g., *Wieser et al*., 2010; *Kallio et al*., 2012], resulting in a significant modification of the plasma flow that reaches the surface, creating a central decrease or even void of ion precipitation and, in the surrounding region, an enhanced ion flux. In Figures 5a and 5b, the decreases in the ENA fluxes seem shifted from the locations of nearby magnetic anomalies. Considering the orbit geometry (Figure 2), these shifts are in the direction away from the incoming plasma. The plasma is deviated and screened off by the stretched minimagnetospheres, forming plasma wakes as suggested by Lunar Prospector observations [*Lin et al*., 1998; *Halekas et al*., 2008], and simulations by *Harnett and Winglee* [2002]. This phenomenon is particularly pronounced during period P1, corresponding to the terminator orbits, where the plasma dynamic pressure toward the lunar surface is lower [cf. *Russell and Lichtenstein*, 1975; *Halekas et al.,* 2008]. The situation is also very similar to recent simulation results of a magnetic anomaly near the lunar terminator by *Zimmerman et al.* [2015].

Figure 4 shows that the reflection fraction during P2 is, like in P1, generally also lower than 20%, and almost half the time lower than 10%. The generally lower scattering fraction is discussed in the first paragraph of this section. In addition to that, there are stronger reductions marked as (5) and (6) in Figures 4 and 5. From Figure 5, we find that these reductions do not appear confined to specific regions, unlike the decreases in P1. Instead, they are probably due to uncertainties in the measurements of the upstream plasma, as Kaguya is (2–4) 10^3 km away from Chandrayaan-1. The differences in the upstream plasma between the spacecraft locations could be related to the proximity of the Moon to the terrestrial magnetopause or the 100 km–1000 km scale variations in the lunar plasma environment due to reflected protons [e.g., *Halekas et al*., 2013; *Fatemi et al*., 2014; *Harada et al*., 2015].

The modeled energy spectrum (Figure 1b) becomes broader and less peaked with increasing plasma temperature. This trend was also observed by *Allegrini et al.* [2013], using IBEX observations. While the trend is clearly seen, the difference is small between ENA spectra generated by an almost monoenergetic incident beam and a fully thermalized incident plasma. When we compare our convolved model (equation (7)) to the observations presented herein (Figure 6), we find that the modeled energy spectra are qualitatively very similar to the observed spectra for both P1 and P2. When the proton thermal speed is comparable to the bulk speed (more noticeable in P2, where the bulk speed is lower), the model by *Futaana et al.* [2012] (F2012(v_b)) predicts a lower ENA energy than what is observed. Here we used the bulk speed v_b. However, if we use the proton mean speed v_m instead of the bulk speed (F2012(v_m)), we get a better match between the F2012 model and the magnetosheath observations. On the other hand, the tails of the spectrum may still be better represented using the convolved model (equation (7)). We can also test these models by comparing to ENA scattering in the plasma sheet [*Harada et al*., 2014]. From their plasma observations, we take $v_b = 0$ and $kT = 573$ eV. Thus, from equation (13), we get $v_{sw} = (0 + 3{\cdot}573\ \mathrm{eV}\ q_e/m_p)^{0.5} = 406$ km/s, which from equation (3) gives an expected $kT_{ENA} = 109$ eV, which is very close to the 107 eV observed by *Harada et al.* [2014]. This simple approach predicts an ENA spectrum similar to the "solar wind" model ($v_b = 400$ km/s) in Figure 1b, while the more advanced convolved model predicts a spectrum similar to the "plasma sheet" model ($kT = 600$ eV). Figures 1b and 6 show the similarities (the spectrum peak/characteristic energy) and differences (the spectrum tails/shape) between these approaches.

As the decreases in the ENA scattering fraction in P1 are attributed to shielding by lunar magnetic anomalies, data in Figures 6a–6c allow us to investigate any spectral changes of the ENAs scattered from these partially shielded regions. However, we do not observe spectral changes even at locations where most of the plasma

is prevented from reaching the surface (Figure 6c). There is no significant shift of the observed spectra toward lower energies compared to the model results. Thus, we do not see any indication of a deceleration by hundreds of eV of the incident ions by electric fields such as those observed at the Moon in the solar wind by e.g., *Saito et al.* [2012] and *Futaana et al.* [2013], modeled by several recent studies [e.g., *Poppe et al*., 2012; *Kallio et al*., 2012; *Jarvinen et al*., 2014; *Deca et al*., 2014, 2015; *Fatemi et al*., 2015; *Giacalone and Hood*, 2015; *Zimmerman et al*., 2015], and observed in laboratory [e.g., *Bamford et al.*, 2012; *Howes et al*., 2015; *Wang et al*., 2012, 2013]. Notably, most of the cited studies concern primarily the low solar zenith angle case, while the case we observe in P1 is at high solar zenith angles. *Zimmerman et al.* [2015] investigated both low and high solar zenith angles. The apparent lack of a strong electric potential at the void regions in our observations can be explained consistently with the results from *Zimmerman et al.* [2015, ff. 2,3,6,7], by the following scenario: The electrostatic deflection of the protons is concentrated to immediate vicinity of the magnetic anomaly [cf. *Futaana et al*., 2013], while as discussed before, we are here mainly observing the downstream wake resulting from the interaction at the anomaly; i.e., the largest voids seen in Figures 5a and 5b are hundreds of kilometers downstream of the magnetic anomalies such as the Stöfler (~40°S, 5°E) and Descartes (~10°S, 15°E) magnetic anomalies that are likely to have created the voids. Although protons may be decelerated by an electric field near the magnetic anomaly, they are accelerated again after deflection when they leave the interaction region, and the protons that impact the lunar surface in the anomaly's wake have retained their original speed.

In P2, most of the decreases of the scattering fraction are attributed to uncertainties in the upstream conditions or low CENA count rates rather than physical characteristics. This may explain the lack of spectral changes in Figures 6e–6h.

5. Conclusions

We adapted existing models for ENA scattering from the lunar regolith [*Schaufelberger et al*., 2011; *Futaana et al*., 2012], to account for the temperature of the incident ion distribution. The adapted (convolved) models describe the broadening of the scattered hydrogen ENA energy spectrum and the directional scattering function as the plasma temperature increases (Figures 1b and 1c). The broadening is qualitatively consistent with previous observations in the magnetosheath [*Allegrini et al*., 2013] and in the plasma sheet [*Harada et al*., 2014] and with the observations studied herein. We also find that we can use simpler models with similar results as the convolved models: The energy spectrum can be approximated using the model by *Futaana et al.* [2012] if the mean speed is used as the model input, with only a slight underestimation of the intensity at the lowest and highest energies of the distribution (Figure 6). The ENA scattering at low SZA (PZA) is close to isotropic [*Schaufelberger et al*., 2011]; even more so in the magnetosheath case (Figure 1c) because of the wider angular distribution of the incident protons. The model results suggest that for hot plasma at high SZA (Figures 7a–7c), an isotropic assumption may be more appropriate than the scattering function derived for solar wind plasma by *Schaufelberger et al.* [2011]. Care must be taken in the interpretation of scattering fractions at high SZA in the magnetosheath because the results vary greatly depending on the scattering model.

Lunar magnetic anomalies are visible in Figure 5 as strong decreases in the ENA reflection fraction, seen clearly in P1 but not unambiguously identified in P2. We explain the stronger effect in P1 by an increased influence of lunar crustal fields toward higher solar zenith angles. To explain Figure 5, we also suggest a downstream shift of the plasma voids formed from the lunar magnetic anomalies. These explanations are in agreement with previous studies [e.g., *Halekas et al*., 2008; *Zimmerman et al*., 2015]. The present ENA images of magnetic anomalies in the magnetosheath are quantitatively and qualitatively different from the previous ENA images obtained in the solar wind [e.g., *Futaana et al*., 2013], but we are observing different magnetic anomalies, at different bulk incidence angles and different upstream plasma conditions. Thus, further data analysis and modeling studies are required to isolate the effect of the plasma temperature and determine how the morphology of the plasma interaction with magnetic anomalies changes in the magnetosheath (and in the plasma sheet) [see also *Harada et al*., 2014], compared to the simple, monoenergetic solar wind case.

The present study expands the ENA scattering efficiency map obtained by *Vorburger et al.* [2013] by reaching further into the lunar nearside, a region that is mostly exposed to magnetosheath plasma rather than undisturbed solar wind. The new area contains both mare and highland regions, but there was no discernable

difference between them. An important implication of the latter conclusion is that the same ENA scattering model can be used for these lunar surfaces. We observe a scattering efficiency on the order of 10%. Although we see several strong decreases in the scattering efficiency, we have attributed these to other causes. From our investigation of the ENA scattering efficiency, we suggest that the scattering process of individual particles remains unchanged in the magnetosheath, and we suggest that different estimates for the scattering fraction from different studies are rather an effect of the choice of scattering model.

Acknowledgments
This work was supported by the Swedish National Space Board (Dnr 97/11). The JSPS (Japan Society for the Promotion of Science) Summer Program 2014 supported the visit of C.L. to Japan dedicated to this multispacecraft, collaborative work. The work by P.W. was supported by the Swiss National Science Foundation. The Clementine lunar albedo data were provided courtesy of the U.S. Naval Research Laboratory (www.nrl.navy.mil/clementine). The Chandrayaan-1/SARA data are available at the Indian Space Science Data Center (ISSDC, http://www.issdc.gov.in/chandrayaan1.html), and the Kaguya/MAP-PACE data are available at the Kaguya Data Archive (http://l2db.selene.darts.isas.jaxa.jp/index.html.en).

References

Allegrini, F., et al. (2013), Lunar energetic atom (ENA) spectra measured by the interstellar boundary explorer (IBEX), *Planet. Space Sci.*, *85*, 232–242, doi:10.1016/j.pss.2013.06.014.

Bamford, R. A., B. Kellett, W. J. Bradford, C. Norberg, A. Thornton, K. J. Gibson, I. A. Crawford, L. Silva, L. Gargaté, and R. Bingham (2012), Minimagnetospheres above the lunar surface and the formation of lunar swirls, *Phys. Rev. Lett.*, *109*, 081101, doi:10.1103/PhysRevLett.109.081101.

Carron, N. J. (2007), *An Introduction to the Passage of Energetic Particles Through Matter*, CRC Press, Boca Raton.

Deca, J., A. Divin, G. Lapenta, B. Lembège, S. Markidis, and M. Horányi (2014), Electromagnetic particle-in-cell simulations of the solar wind interaction with lunar magnetic anomalies, *Phys. Rev. Lett.*, *112*, 151102, doi:10.1103/PhysRevLett.112.151102.

Deca, J., A. Divin, B. Lembège, M. Horányi, S. Markidis, and G. Lapenta (2015), General mechanism and dynamics of the solar wind interaction with lunar magnetic anomalies from 3-D PIC simulations, *J. Geophys. Res. Space Physics*, *120*, 6443–6463, doi:10.1002/2015JA021070.

Fairfield, D. H. (1971), Average and unusual locations of the Earth's magnetopause and bow shock, *J. Geophys. Res.*, *76*, 6700–6716, doi:10.1029/JA076i028p06700.

Fatemi, S., M. Holmström, Y. Futaana, C. Lue, M. R. Collier, S. Barabash, and G. Stenberg (2014), Effects of protons reflected by lunar crustal magnetic fields on the global lunar plasma environment, *J. Geophys. Res. Space Physics*, *119*, 6095–6105, doi:10.1002/2014JA019900.

Fatemi, S., C. Lue, M. Holmström, A. R. Poppe, M. Wieser, S. Barabash, and G. T. Delory (2015), Solar wind plasma interaction with Gerasimovich lunar magnetic anomaly, *J. Geophys. Res Space Physics*, *120*, 4719–4735, doi:10.1002/2015JA021027.

Formisano, V., G. Moreno, F. Palmiotto, and P. C. Hedgecock (1973), Solar wind interaction with the Earth's magnetic field 1. Magnetosheath, *J. Geophys. Res.*, *78*(19), 3714–3730, doi:10.1029/JA078i019p03714.

Funsten, H. O., et al. (2013), Reflection of solar wind hydrogen from the lunar surface, *J. Geophys. Res. Planets*, *118*, 292–305, doi:10.1002/jgre.20055.

Futaana, Y., S. Barabash, M. Holmström, and A. Bhardwaj (2006), Low energy neutral atoms imaging of the Moon, *Planet. Space Sci.*, *54*(2), 132–143, doi:10.1016/j.pss.2005.10.010.

Futaana, Y., S. Barabash, M. Wieser, M. Holmström, C. Lue, P. Wurz, A. Schaufelberger, A. Bhardwaj, M. B. Dhanya, and K. Asamura (2012), Empirical energy spectra of neutralized solar wind protons from the lunar regolith, *J. Geophys. Res.*, *117*, E05005, doi:10.1029/2011JE004019.

Futaana, Y., S. Barabash, M. Wieser, C. Lue, P. Wurz, A. Vorburger, A. Bhardwaj, and K. Asamura (2013), Remote energetic neutral atom imaging of electric potential over a lunar magnetic anomaly, *Geophys. Res. Lett.*, *40*, 262–266, doi:10.1002/grl.50135.

Giacalone, J., and L. L. Hood (2015), Hybrid simulations of the interaction of solar wind protons with a concentrated lunar magnetic anomaly, *J. Geophys. Res. Space Physics*, *120*, 4081–4094, doi:10.1002/21014JA020938.

Halekas, J. S., G. T. Delory, D. A. Brain, R. P. Lin, and D. L. Mitchell (2008), Density cavity observed over a strong lunar crustal magnetic anomaly in the solar wind: A mini-magnetosphere?, *Planet. Space Sci.*, *56*, 941–946, doi:10.1016/j.pss.2008.01.008.

Halekas, J. S., A. R. Poppe, J. P. McFadden, and K.-H. Glassmeier (2013), The effects of reflected protons on the plasma environment of the moon for parallel interplanetary magnetic fields, *Geophys. Res. Lett.*, *40*, 4544–4548, doi:10.1002/grl.50892.

Harada, Y., et al. (2014), Backscattered energetic neutral atoms from the Moon in the Earth's plasma sheet observed by Chandarayaan-1/sub-keV atom reflecting analyzer instrument, *J. Geophys. Res. Space Physics*, *119*, 3573–3584, doi:10.1002/2013JA019682.

Harada, Y., J. S. Halekas, A. R. Poppe, Y. Tsugawa, S. Kurita, and J. P. McFadden (2015), Statistical characterization of the foremoon particle and wave morphology: ARTEMIS observations, *J. Geophys. Res. Space Physics*, *120*, 4907–4921, doi:10.1002/2015JA021211.

Harnett, E. M., and R. M. Winglee (2002), 2.5D particle and MHD simulations of mini-magnetospheres at the Moon, *J. Geophys. Res.*, *107*(A12), 1421, doi:10.1029/2002JA009241.

Howes, C. T., X. Wang, J. Deca, and M. Horányi (2015), Laboratory investigation of lunar surface electric potentials in magnetic anomaly regions, *Geophys. Res. Lett.*, *42*, 4280–4287, doi:10.1002/2015GL063943.

Jarvinen, R., M. Alho, E. Kallio, P. Wurz, S. Barabash, and Y. Futaana (2014), On vertical electric fields at lunar magnetic anomalies, *Geophys. Res. Lett.*, *41*, 2243–2249, doi:10.1002/2014GL059788.

Kallio, E., et al. (2012), Kinetic simulations of finite gyroradius effects in the lunar plasma environment on global, meso, and microscales, *Planet. Space Sci.*, *74*, 146–155, doi:10.1016/j.pss.2012.09.012.

Kazama, Y., S. Barabash, M. Wieser, K. Asamura, and P. Wurz (2007), Development of an LENA instrument for planetary missions by numerical simulations, *Planet. Space Sci.*, *55*(11), 1518–1529, doi:10.1016/j.pss.2006.11.027.

Lin, R. P., D. L. Mitchell, D. W. Curtis, K. A. Anderson, C. W. Carlson, J. McFadden, M. H. Acuña, L. L. Hood, and A. Binder (1998), Lunar surface magnetic fields and their interaction with the solar wind: Results from lunar prospector, *Science*, *281*, 1480–1484, doi:10.1126/science.281.5382.1480.

Lue, C., Y. Futaana, S. Barabash, M. Wieser, M. Holmström, A. Bhardwaj, M. B. Dhanya, and P. Wurz (2011), Strong influence of lunar crustal fields on the solar wind flow, *Geophys. Res. Lett.*, *38*, L03202, doi:10.1029/2010GL046215.

Lue, C., Y. Futaana, S. Barabash, M. Wieser, A. Bhardwaj, and P. Wurz (2014), Chandrayaan-1 observations of backscattered solar wind protons from the lunar regolith: Dependence on the solar wind speed, *J. Geophys. Res. Planets.*, *119*, 968–975, doi:10.1002/2013JE004582.

McCann, D., S. Barabash, H. Nilsson, and A. Bhardwaj (2007), Miniature ion mass analyzer, *Planet. Space Sci.*, *55*, 1190–1196, doi:10.1016/j.pss.2006.11.020.

McComas, D. J., et al. (2009), Lunar backscatter and neutralization of the solar wind: First observations of neutral atoms from the Moon, *Geophys. Res. Lett.*, *36*, L12104, doi:10.1029/2009GL038794.

Poppe, A. R., J. S. Halekas, G. T. Delory, and W. M. Farrell (2012), Particle-in-cell simulations of the solar wind interaction with lunar crustal magnetic anomalies: Magnetic cusp regions, *J. Geophys. Res.*, *117*, A09105, doi:10.1029/2012JA017844.

Purucker, M. E., and J. B. Nicholas (2010), Global spherical harmonic models of the internal magnetic field of the Moon based on sequential and coestimation approaches, *J. Geophys. Res.*, *115*, E12007, doi:10.1029/2010JE003650.

Rodríguez, M. D. F., L. Saul, P. Wurz, S. A. Fuselier, H. O. Funsten, D. J. McComas, and E. Möbius (2012), IBEX-Lo observations of energetic neutral hydrogen atoms originating from the lunar surface, *Planet. Space Sci.*, *60*(1), 297–303, doi:10.1016/j.pss.2011.09.009.

Russell, C. T., and B. R. Lichtenstein (1975), On the source of lunar limb compressions, *J. Geophys. Res.*, *80*, 4700–4711, doi:10.1029/JA080i034p04700.

Saito, Y., et al. (2008), Solar wind proton reflection at the lunar surface: Low energy ion measurement by MAP-PACE onboard SELENE (KAGUYA), *Geophys. Res. Lett.*, *35*, L24205, doi:10.1029/2008GL036077.

Saito, Y., et al. (2010), In-flight performance and initial results of Plasma Energy Angle and Composition Experiment (PACE) on SELENE (Kaguya), *Space Sci. Rev.*, *154*(1–4), 265–303, doi:10.1007/s11214-010-9647-x.

Saito, Y., M. N. Nishino, M. Fujimoto, T. Yamamoto, S. Yokota, H. Tsunakawa, H. Shibuya, M. Matsushima, H. Shimizu, and F. Takahashi (2012), Simultaneous observation of the electron acceleration and ion deceleration over lunar magnetic anomalies, *Earth Planets Space*, *64*, 83–92.

Saul, L., et al. (2013), Solar wind reflection from the lunar surface: The view from far and near, *Planet. Space Sci*, *84*, 1–4, doi:10.1016/j.pss.2013.02.004.

Schaufelberger, A., P. Wurz, S. Barabash, M. Wieser, Y. Futaana, M. Holmström, A. Bhardwaj, M. B. Dhanya, R. Sridharan, and K. Asamura (2011), Scattering function for energetic neutral hydrogen atoms off the lunar surface, *Geophys. Res. Lett.*, *38*, L22202, doi:10.1029/2011GL049362.

Shue, J.-H., J. K. Chao, H. C. Fu, C. T. Russell, P. Song, K. K. Khurana, and H. J. Singer (1997), A new functional form to study the solar wind control of the magnetopause size and shape, *J. Geophys. Res.*, *102*(A5), 9497–9511, doi:10.1029/97JA00196.

Vorburger, A., P. Wurz, S. Barabash, M. Wieser, Y. Futaana, M. Holmström, A. Bhardwaj, and K. Asamura (2012), Energetic neutral atom observations of magnetic anomalies on the lunar surface, *J. Geophys. Res.*, *117*, A07208, doi:10.1029/2012JA017553.

Vorburger, A., P. Wurz, S. Barabash, M. Wieser, Y. Futaana, C. Lue, M. Holmström, A. Bhardwaj, M. B. Dhanya, and K. Asamura (2013), Energetic neutral atom imaging of the lunar surface, *J. Geophys. Res. Space Physics*, *118*, 3937–3945, doi:10.1002/jgra.50337.

Vorburger, A., P. Wurz, S. Barabash, M. Wieser, Y. Futaana, A. Bhardwaj, and K. Asamura (2015), Imaging the South Pole-Aitken basin in backscattered neutral hydrogen atoms, *Planet. Space Sci.*, *115*, 57–63, doi:10.1016/j.pss.2015.02.007.

Wang, X., M. Horányi, and S. Robertson (2012), Characteristics of a plasma sheath in a magnetic dipole field: Implications to the solar wind interaction with the lunar magnetic anomalies, *J. Geophys. Res.*, *117*, A06226, doi:10.1029/2012JA017635.

Wang, X., C. T. Howes, M. Horányi, and S. Robertson (2013), Electric potentials in magnetic dipole fields normal and oblique to a surface in plasma: Understanding the solar wind interaction with lunar magnetic anomalies, *Geophys. Res. Lett.*, *40*, 1686–1690, doi:10.1002/grl.50367.

Wieser, M., S. Barabash, Y. Futaana, M. Holmström, A. Bhardwaj, R. Sridharan, M. B. Dhanya, P. Wurz, A. Schaufelberger, and K. Asamura (2009), Extremely high reflection of solar wind protons as neutral hydrogen atoms from regolith in space, *Planet. Space Sci.*, *57*(14–15), 2132–2134, doi:10.1016/j.pss.2009.09.012.

Wieser, M., S. Barabash, Y. Futaana, M. Holmström, A. Bhardwaj, R. Sridharan, M. B. Dhanya, A. Schaufelberger, P. Wurz, and K. Asamura (2010), First observation of a mini-magnetosphere above a lunar magnetic anomaly using energetic neutral atoms, *Geophys. Res. Lett.*, *37*, L05103, doi:10.1029/2009GL041721.

Zimmerman, M. I., W. M. Farrell, and A. R. Poppe (2015), Kinetic simulations of kilometer-scale mini-magnetosphere formation on the Moon, *J. Geophys. Res. Planets*, *120*, 1893–1903, doi:10.1002/2015JE004865.